Stability, Receptivity, and Sensitivity Analyses of Buffeting Transonic Flow over a Profile

Fulvio Sartor*
University of Liverpool, Liverpool, England L63 3GH, United Kingdom
Clément Mettot†
Saint-Gobain Recherche, 93300 Aubervilliers, France
and
Denis Sipp‡
ONERA–The French Aerospace Lab, 92190 Meudon, France

DOI: 10.2514/1.J053588

A transonic flow over the OAT15A supercritical profile is considered. The interaction between the shock wave and the turbulent boundary layer is investigated through numerical simulation and global stability analysis for a wide range of angles of attack. Numerical simulations are in good agreement with previous studies and manage to reproduce the high-amplitude self-sustained shock oscillations known as shock buffet. In agreement with previous results, it is found that the buffet phenomenon is driven by an unstable global mode of the linearized Navier–Stokes equations. Analysis of the adjoint global mode reveals that the flow is most receptive to harmonic forcings on the suction side of the profile, within the boundary layer upstream of the shock foot, in the recirculation bubble downstream of the shock foot, and on the right characteristic that impinges the shock foot. An eigenvalue sensitivity analysis shows that a steady streamwise force applied either in the boundary layer or in the recirculation region, a steady cooling of the boundary layer, or a steady source of eddy viscosity (a mechanical vortex generator for example) all lead to stabilization of the buffet mode. Finally, pseudoresonance phenomena have been analyzed by performing a singular-value decomposition of the global resolvent, which revealed that, besides the low-frequency shock unsteadiness, the flow also undergoes medium-frequency unsteadiness, linked to Kelvin–Helmholtz-type instability. Such results are reminiscent of the medium-frequency perturbations observed in more traditional shock wave/boundary-layer interactions.

I. Introduction

SHOCK waves almost inevitably occur when dealing with supersonic flows. The presence of shock waves entails the existence of discontinuities and regions of high gradients, which are the shocks themselves, and the shear layers resulting from the interaction with the boundary layers developing over a surface [1]. The interaction between the shock and the boundary layer can have a significant influence on aircraft or rocket performance and often leads to undesirable effects [2]. Considering a flow over a wing, a strong interaction between the shock and the boundary layers may lead to catastrophic separation: the consequence can be the occurrence of large-scale unsteadiness [3], such as high-amplitude self-sustained shock movements, known as shock buffet. This phenomenon presents an industrial interest, and it has therefore been the subject of numerous studies in the past [4].

The buffet unsteadiness is a strong phenomenon that can be observed in a two-dimensional transonic flow over a profile: it is known [5,6] that, for a combination of Mach numbers and angles of attack, the shock unsteadiness dominates the interaction. In the particular two-dimensional case, the unsteadiness is characterized by periodic low-frequency shock motions, which are maintained with no external force [7]. However, the periodic motions occur at timescales that are much longer than those of the wall-bounded turbulence, so a numerical simulation performed solving Reynolds-averaged Navier–Stokes (RANS) equations closed with a turbulence model may be justified. Insofar, recent numerical studies have revealed that unsteady RANS simulations can successfully reproduce the buffet unsteadiness using various turbulence models [8–11]. When comparing results obtained on the same configuration but using different turbulence models, the main difference that can be observed is in the shock-induced separated zone. The shock motions have been found to be strongly dependent on this particular zone, and for this reason, a different turbulence model can lead to a different unsteady prediction. Despite some discrepancies with experimental investigations on the critical angle of attack that determines the buffet onset, numerical simulations provide a complete description of the low-frequency shock motions.

However, besides the shock unsteadiness, a shock-wave/boundary-layer interaction (SWBLI) may present medium-frequency unsteadiness caused by the separated zone: it is well established [12] that the interaction between a shock wave and a boundary layer is characterized by low- and medium-frequency unsteadiness. RANS and unsteady RANS (URANS) simulations fail to predict the medium-frequency unsteadiness, probably linked to Kelvin–Helmholtz-type instabilities, and a different approach is needed in order to fully characterize the flow dynamics. As is commonly done in SWBLI [13], one can introduce a dimensionless frequency (or Strouhal number) defined as

$$S_L = \frac{fL}{U_e} \tag{1}$$

where f is the frequency, L is a characteristic length of the order of the separated zone, and U_e a characteristic velocity above the recirculation bubble. For the buffeting over an airfoil, we choose L as the chord c of the airfoil and U_e as the velocity in the freestream U_∞. In other SWBLI configurations, it has been shown [12] that a typical value of $S_L = 0.02 - 0.05$ describes qualitatively well the shock motions, whereas a value of $S_L = 0.1 - 0.5$ is typical for medium-frequency motions of the mixing layer.

Received 30 April 2014; revision received 31 August 2014; accepted for publication 10 September 2014; published online 16 December 2014.

*Research Associate, School of Engineering; fulvio.sartor@liverpool.ac.uk.
†Research Engineer, 39 Quai Lucien Lefranc.
‡Research Scientist, Fundamental and Experimental Aerodynamics Department, 8 rue des Vertugadins.

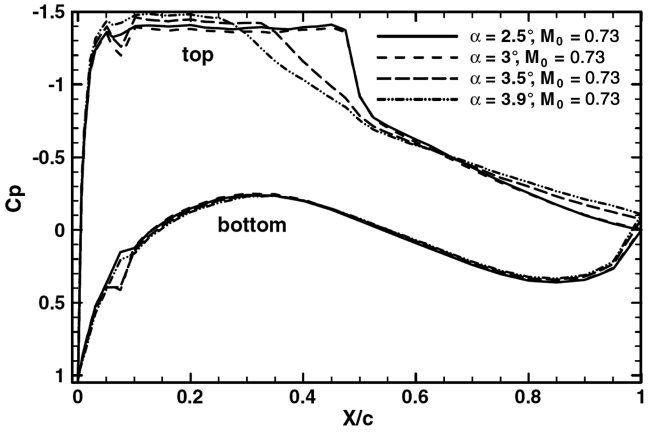

Fig. 1 Pressure coefficient distribution. Experimental investigation from Jacquin et al. [22].

Linear-stability analysis has become a tool commonly used in fluid dynamics, which can often give physical insight to understand flow unsteadiness [14,15]. According to Huerre [16], occurrences of unsteadiness can be classified into two main categories: the flow can behave as an oscillator, in which case an absolute instability imposes its own dynamics; or it can behave as a noise amplifier, in which case the system filters and amplifies existing environmental noise, due to convective instabilities. In the first case, a global-mode decomposition has the ability to identify the mechanism responsible for the self-sustained unsteadiness, indicating that the flow is driven by an unstable global mode. In the second case, the unsteadiness is usually characterized by a broadband spectrum, and the flow does not exhibit any unstable global mode. The linearized Navier–Stokes operator then acts as a linear filter of the external environment, and a frequency-selection mechanism leads to a broadband spectrum: the eigenvalue decomposition poorly describes the dynamics of the phenomenon [14,17]. Flows without an unstable global mode can nonetheless possess a weakly damped, stable global mode that may lead to a slightly peaky spectrum when forced by random noise. In such cases, a singular-value decomposition of the resolvent operator highlights pseudoresonance phenomena, which are more suitable to describe the dynamics of a globally stable flow.

In a transonic flow over a NACA0012 profile configuration, Crouch et al. [18] performed a global stability analysis and found a strong link between the onset of shock unsteadiness and the appearance of an unstable global mode. It has been shown that, for a given Mach number, a critical value of the angle of attack exists, above which the shock starts to oscillate, in the same way that a critical Reynolds number is responsible for vortex shedding in a cylinder wake [19]. In this paper, we consider a similar approach, and we extend the work by solving the associated adjoint problem and by computing the sensitivity gradient of the unstable eigenvalue, in order to find regions of the flow where a steady [20] or harmonic [21] control should be placed to reduce the buffet phenomenon intensity. We will finally also analyze the pseudoresonance phenomena in the flow that generally also occur in SWBLI at medium frequencies: for this, we perform a singular-value decomposition of the global resolvent and highlight frequencies that yield the strongest response with respect to external forcings.

The paper proceeds as follows. The OAT15A profile configuration, which has been experimentally investigated by Jacquin et al. [22], is presented in Sec. II. Then, a wide range of angles of attack is numerically investigated by means of RANS and URANS simulations (Sec. III), spanning from $\alpha = 2.5$ deg to $\alpha = 7.0$ deg. In Sec. IV, we will show how direct global modes may describe the main features of the flow, how the adjoint global modes may yield valuable information to analyze the receptivity of the flow, and how a sensitivity analysis may predict beforehand where an actuator should be placed to suppress the buffet phenomenon. Then, in Sec. V, we perform a singular-value decomposition of the global resolvent in order to highlight the pseudoresonance phenomena that may occur at medium frequencies. Section VI concludes the paper with a summary of the major findings.

II. Experimental Investigation

The experiments were conducted in the transonic S3Ch wind tunnel of ONERA–The French Aerospace Lab, a continuous closed-loop facility powered by a 3500 kW two-stage fan. The model is an OAT15A supercritical aerofoil characterized by a $c = 0.23$ m chord length, a relative thickness of 12.3%, and a 0.78 m span. The central region of the wing is equipped with 68 static pressure taps and 36 unsteady Kulite transducers. In their investigation, Jacquin et al. [22] considered several combinations of Mach number and angles of attack, adjusted by means of adaptable walls. In the numerical study, we will only consider $M = 0.73$ with variation of the incidence α. The stagnation conditions were near ambient pressure and temperature, and the Reynolds number based on the chord length was around $Re_c = 3 \times 10^6$. The boundary-layer transition was triggered on the model using a carborundum strip located at $x/c = 0.07$ from the leading edge.

Figure 1 shows the mean distribution of the wall pressure coefficient C_p around the profile for four angles of attack. The upper part of the curves, which corresponds to the suction side of the profile, is characterized by a pressure plateau before the compression caused by the shock. Starting from $\alpha = 3.5$ deg, this pressure jump is smeared out along the profile, indicating an unsteady position of the shock. In Fig. 1, one can also observe the effect of the carborundum strips located at $x/c = 0.07$ (on both pressure and suction sides of the profile), which create a compression wave particularly visible in the schlieren image of Fig. 2.

The buffet onset can also be noticed from the power spectral density of pressure in Fig. 3: for $\alpha = 3.0$ deg, the shock is steady, with the signal energy remaining low and distributed among all frequencies. However, a small bump can be detected between 40 and 100 Hz, with the amplitude of this bump increasing with the angle of

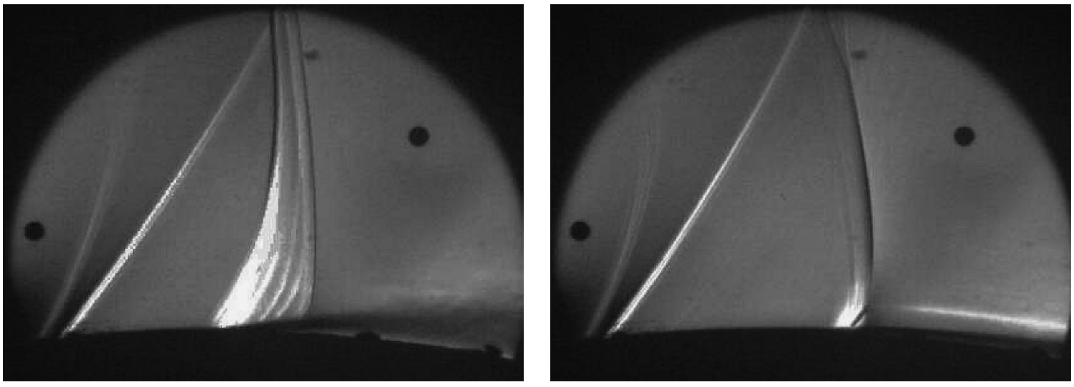

a) Shock at the most upstream location **b) Shock at the most downstream location**

Fig. 2 Instantaneous schlieren images from Jacquin et al. [22].

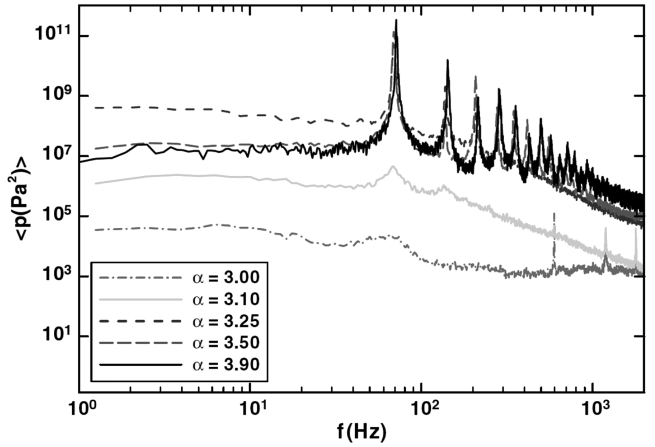

Fig. 3 Power spectrum of pressure at $x/c = 0.45$. From Jacquin et al. [22].

attack. For higher values of α, the bump becomes narrower and a peak that corresponds to the buffet frequency ($f = 69$ Hz) is visible from $\alpha = 3.25$ deg. When increasing the angle of attack, the peak frequency remains at $f = 69$ Hz, indicating that the buffet frequency does not depend on the angle of attack. On the contrary, as also shown by other studies [5,7], the buffet frequency is sensitive to the upstream Mach number. Unfortunately, the experimental studies focused only on the low-frequency unsteadiness; none of the spectra presented by Jacquin et al. [22] yielded any information about a possible medium-frequency bump in the premultiplied spectra, as usually observed in other SWBLIs.

Figure 2 shows the instantaneous schlieren images for the two extreme shock positions when the buffet phenomenon is observed: here, at $\alpha = 3.5$ deg. On both images, one can recognize the shock wave with the classical lambda pattern. When the shock is in the most upstream position (Fig. 2a), the separation regions covers half of the profile, and the recirculation bubble can be recognized by a bright zone close to the profile under the mixing layer (the darker zone that starts at the shock foot). When the shock is in the most downstream position (Fig. 2b), the separation is smaller, and the shock is better captured by the schlieren image because of less three-dimensional effects.

Independent of the shock position, the compression wave caused by the carborundum strip is always visible on the schlieren image, starting from the profile at $x/c = 0.07$. Slightly upstream, one can recognize in both cases of Fig. 2a bright curved line: as will be shown in the next sections, this is a left characteristic line, which has a central role in the stability of the flow.

III. Base Flows and Unsteady Nonlinear Simulations

The numerical simulations were performed using RANS equations, solved with the elsA v3.3 code [23]. The Spalart–Allmaras turbulence model [24] has been used to provide closure for the averaged Reynolds stresses. The simulations mimic the wind-tunnel testing conditions described in Sec. II, with boundary conditions that match the experimental situation: the stagnation pressure and temperature are 101,325 Pa and 300 K, whereas the Mach number is $M = 0.73$. The OAT15A aerofoil of chord $c = 0.23$ m is modeled as an adiabatic no-slip wall, the boundary layer on the profile is fully turbulent, and the Reynolds number was set to $Re_c = 3.2 \times 10^6$ based on the chord length. The angle of attack has been adjusted by changing the velocity vector components in the far-field condition, given by $u = U_\infty \cos\alpha$ and $v = U_\infty \sin\alpha$, where u and v are the horizontal and vertical velocity components, and $U_\infty = 240.93$ m/s is the reference velocity modulus.

A. Spatial Discretization

We use a two-dimensional structured grid: a C-type mesh where far-field conditions are imposed 44 chords away from the profile. The reference grid is composed of 72,000 cells: 120 nodes in the direction normal to the profile (approximately 40 inside the boundary layer), 90 nodes in the horizontal direction in the wake, and 210 nodes along each side of the profile. The first mesh point in the boundary layer is always below $y^+ = 0.9$ on the profile. Two additional grids have been considered for a mesh convergence study, where we changed the grid refinement in the shock region. Considering the chord length c as a characteristic dimension, the grid definition in the shock region is $\Delta_x/c = 0.003$ for the reference mesh, and $\Delta_x/c = 0.002$ and $\Delta_x/c = 0.001$ for the convergence study.

Figure 4 shows the whole domain used in the numerical investigation: in Fig. 4a, one can see the whole domain, where only one point out of eight is represented along the profile and one point out of four is represented in the direction perpendicular to it for the reference mesh. The shock region displays a constant grid refinement in the streamwise direction: Fig. 4b presents a zoom of the shock region, showing all the grid cells. The grid refinement influences the shock thickness but not the shock location.

A second-order AUSM + (P) upwind scheme is used for the mean convective fluxes [25]. Roe and Jameson schemes were not considered due to poor shock treatment when investigating the stability of the flow. A first-order Roe scheme with Harten's

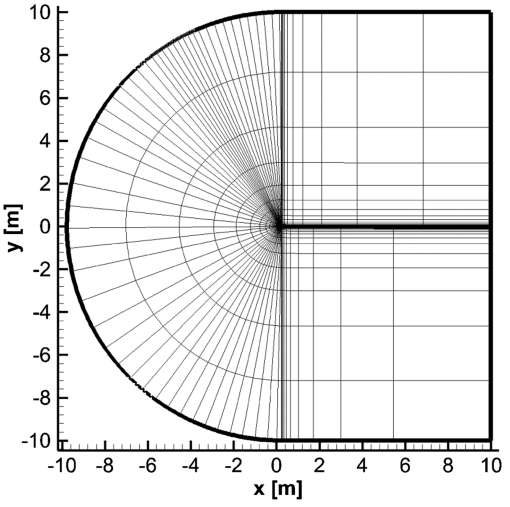

a) Whole domain, showing one point out of eight along the profile and one point out of four in the direction normal to it

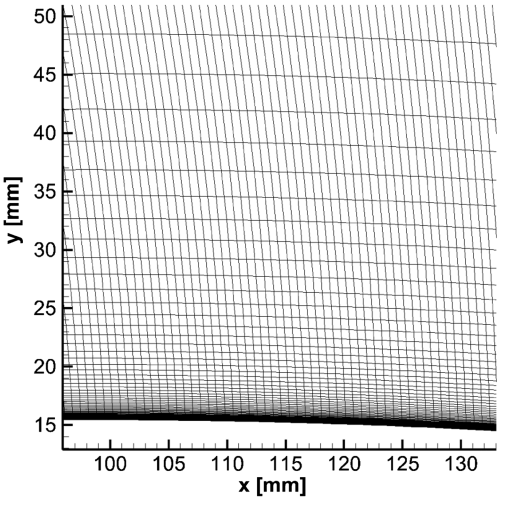

b) Zoom near the shock region, showing all the grid points around $x/c = 0.5$

Fig. 4 Reference mesh used for the numerical simulation and for the stability analysis.

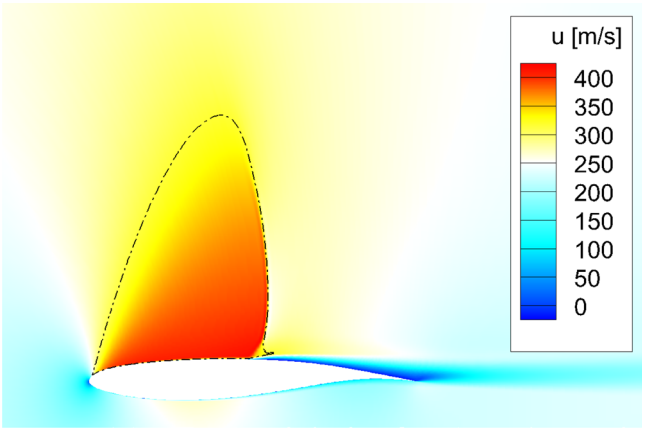

Fig. 5 Horizontal velocity field, with RANS solution at $\alpha = 3.5$ deg (buffet-onset condition).

correction is used for the turbulent convective fluxes, and a second-order central difference scheme is used for the diffusive fluxes.

B. Governing Equations

After spatial discretization, the governing equations can be recast under the following form:

$$\frac{\mathrm{d}\boldsymbol{w}}{\mathrm{d}t} = \mathcal{R}(\boldsymbol{w}) \tag{2}$$

where $\boldsymbol{w} \in \mathbb{R}^N$ represents the set of conservative variables describing the flow at each spatial location of the mesh in the domain Ω, and $\mathcal{R}$: $\Omega \in \mathbb{R}^N \rightarrow \mathbb{R}^N$ is differentiable within Ω and represents the discrete residuals. Steady solutions $\bar{\boldsymbol{w}} \in \mathbb{R}^N$, referred to as base flows, are defined by the equation

$$\mathcal{R}(\bar{\boldsymbol{w}}) = 0 \tag{3}$$

In the examined case, the governing equations contain the Spalart–Allmaras equation; thus, the base flow $\bar{\boldsymbol{w}}$ takes into account the Reynolds stresses involved in the turbulence model.

C. Temporal Discretization

A first-order backward-Euler scheme with local time stepping has been used to converge to the steady-state solutions, whereas unsteady computations were performed using a second-order Gear's formulation with a physical time step fixed at $T_{\mathrm{st}} = 5 \cdot 10^{-7}$ s. This yields a maximum Courant–Friedrichs–Lewy (CFL) number of about 13 in the boundary layer upstream of the shock, 26 in the wake of the aerofoil, and less than one in most of the domain. At least eight Newton subiterations are required at each time step to decrease the norm of the residuals by a factor of 10.

D. Base Flows (RANS)

A set of 10 simulations is performed, imposing different angles of attack, spanning from $\alpha = 2.5$ deg up to $\alpha = 7.0$ deg every $\Delta_\alpha = 0.25$ deg. The maximal Mach numbers (occurring before the shock) associated to the lower and upper values of α correspond to $M = 1.35$ and $M = 1.50$.

Using a local time step with a CFL condition of 10, all computations converge to steady solutions, characterized by explicit residuals that have decreased by at least eight orders of magnitude. Figures 5 and 6 present the horizontal velocity field u and boundary-layer profiles at different chordwise locations for the particular case of $\alpha = 3.5$ deg, which corresponds to the buffet-onset condition (see next).

In Fig. 5, one can notice that the separation region starts at the shock foot and that the recirculation bubble modifies the shape of the shock into a lambda pattern. The reattachment point is fixed to the end of the profile, and thus does not vary with the angle of attack. However, when the angle of attack is very high, the flow does not reattach at all.

Figure 6 presents the wall normal velocity profile across the boundary layer, where the dots indicate the mesh points. Those profiles are obtained at three different streamwise locations, corresponding to $x/c = 0.15$, $x/c = 0.30$, and $x/c = 0.45$, in the supersonic region before the separation occurring at $x/c = 0.50$. In all the cases, one can notice the viscous sublayer and the log region. Regardless of the location, an asymptotic value of $u^+ = 22$ m/s is always reached outside the boundary layer. The boundary layer becomes thicker as it develops along the profile and approaches the shock wave.

Figure 7 shows the pressure coefficient distribution along the profile for various angles of attack. For the smallest angle of attack, the results compare reasonably well with the experimental measurements of Jacquin et al. [22] presented in Sec. II, even if with some difference in the shock position, probably due to the fact that, in the numerical simulation, the trailing edge is sharp. For higher angles of attack, the unsteadiness of the shock wave in the experiment smears out the pressure distribution, which is not observed in the steady base-flow solutions. Yet, in all cases, the distribution of the wall pressure coefficient C_p around the profile is characterized by a pressure plateau before the shock, as in Fig. 1. On the pressure side of the profile, the C_p coefficient does not present a strong dependency on the incidence.

The increase of the angle of attack yields a slight decrease of the pressure coefficient on the suction side of the profile (Fig. 7 presents $-C_p$), and it induces an upstream movement of the shock: a configuration with a high angle of attack will be characterized by a stronger shock that causes a larger recirculation bubble. Figure 8 presents a comparison between two base-flow solutions obtained with the lower and higher angles of attack considered in this study.

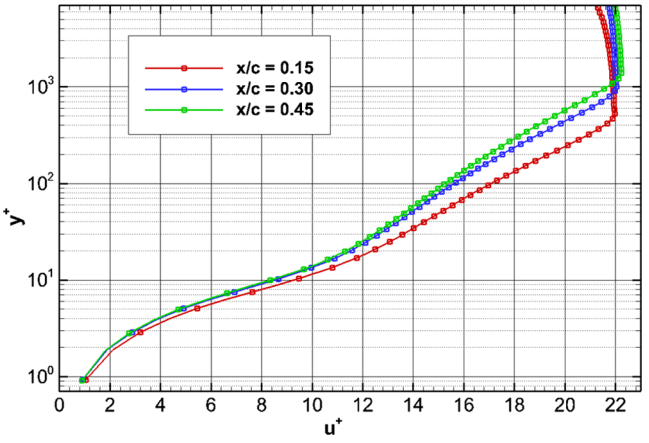

Fig. 6 Boundary-layer profiles, with RANS solution at $\alpha = 3.5$ deg (buffet-onset condition).

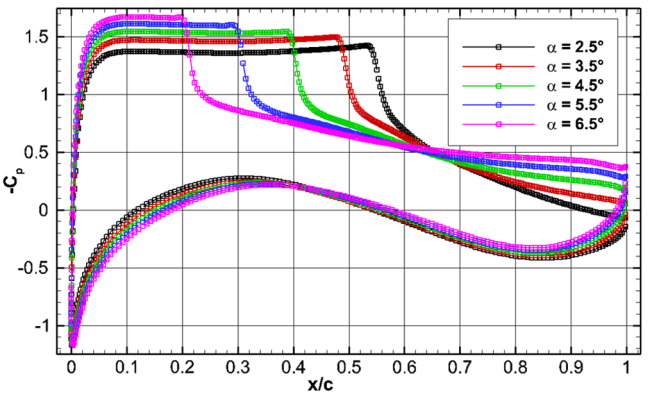

Fig. 7 Pressure coefficient distribution for different angles of attack.

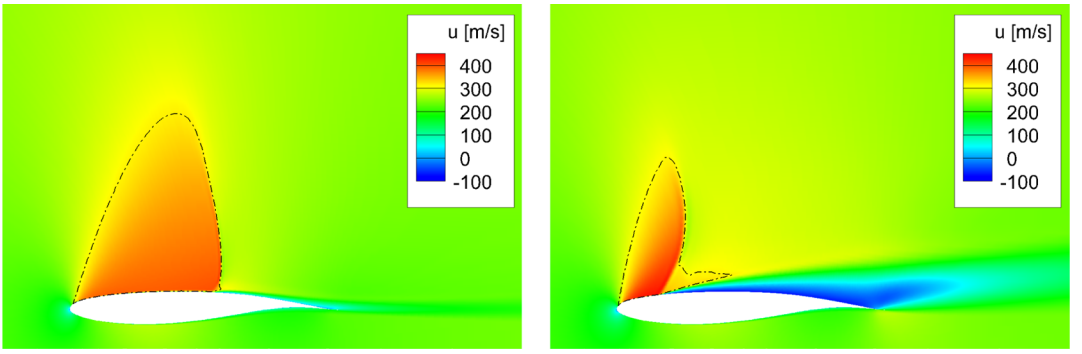

a) Horizontal velocity, $\alpha = 2.5^\circ$ b) Horizontal velocity, $\alpha = 7.0^\circ$

Fig. 8 RANS solution at different angles of attack.

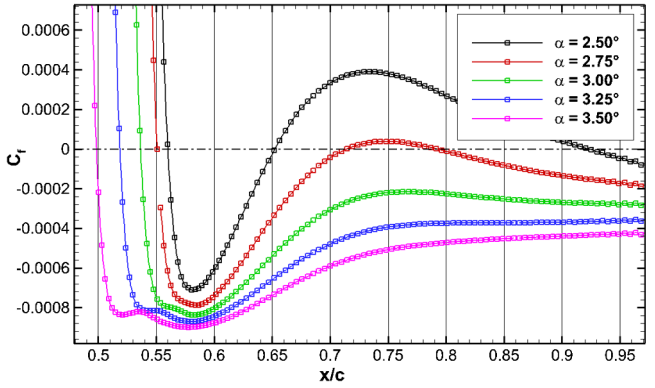

Fig. 9 Skin-friction coefficient distribution for different angles of attack.

The displacement of the separation point as α increases can also be observed in Fig. 9, which presents the distribution of the skin-friction coefficient for angles of attack up to $\alpha = 3.5$ deg.

Two distinct separated regions are visible for $\alpha = 2.5$ deg and $\alpha = 2.75$ deg: one at the shock foot and one at the trailing edge. For $\alpha = 3.0$ deg, the recirculation region extends from the shock foot until the end of the profile. In this case, as will be shown next, the unsteady RANS simulation still converges to the steady-state solution. This behavior is not in agreement with the idea that buffet onset occurs once the separation bubble extends from the shock foot to the trailing edge, as proposed by Pearcey and Holder [26]. As previously stated by Crouch et al. [18], the results do not show a clear link between buffet onset and the qualitative features of the flow separation.

The configurations with angles of attack greater than $\alpha = 4.5$ deg, as the one presented in Fig. 8b, are not commonly investigated because of their limited industrial interest. However, as will be shown in next sections, those configurations are interesting when considered from a stability point of view.

E. Unsteady Nonlinear Simulations (URANS)

URANS computations are initialized with nonconverged RANS solutions, for which the residual 2-norm is about 10^{-3}. When the angle of attack is small, URANS computations converge toward a steady solution, and no unsteady phenomena is observed. Increasing the angle of attack, URANS simulations indicate an unsteady behavior as soon as $\alpha \geq 3.5$ deg: in which case, the shock wave begins to oscillate back and forth with a periodic motion.

Figure 10a presents the time evolution of the lift coefficient for the buffet-onset configuration: after a long transient, a periodic motion sets in that is characterized by a frequency around 77 Hz. The mean value of the lift coefficient exactly coincides with the value obtained solving the steady RANS equations, and it is around $C_z = 0.974$. This indicates that, as the perturbation develops, no mean flow harmonic seems to be generated by the nonlinearities.

Figure 10b presents the same plot but for higher angles of attack: the mean lift coefficients (the steady-state values again always correspond to the mean values obtained on the saturated limit cycles) decrease when increasing the angle of attack (from $C_z = 0.970$ when $\alpha = 4.0$ deg to $C_z = 0.958$ for $\alpha = 4.5$ deg), whereas the amplitudes of the oscillations increase (note the scale changes between Figs. 10a and 10b). When $\alpha = 4.0$ deg, the buffet phenomenon frequency is still at $f = 77$ Hz, but when considering higher angles of attack, the frequency of the unsteady phenomenon slightly increases up to 80 Hz.

It is seen that the transient is shortest when $\alpha = 4.00$ deg: both for $\alpha = 3.50$ deg and $\alpha = 4.50$ deg, the simulations need more time to reach the periodic states. This result is counterintuitive and will be explained next with the stability analysis. The numerical simulations also indicate that, up to $\alpha = 6.0$ deg, the flows remain unsteady: a further increment of the angle of attack then yields simulations that again converge to a steady solution. This phenomenon, known as buffet offset, has been observed in other studies [5,27], but to the

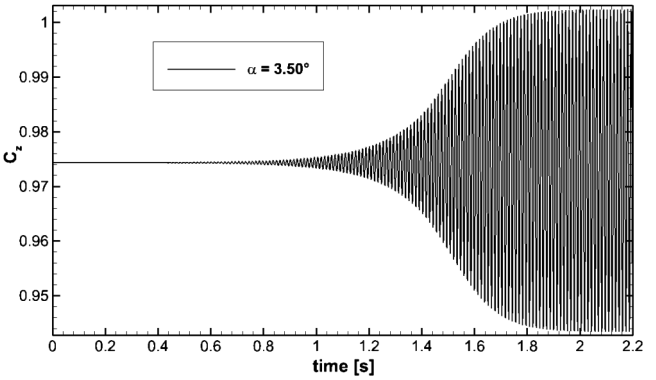

a) Buffet-onset condition ($\alpha = 3.5^o$)

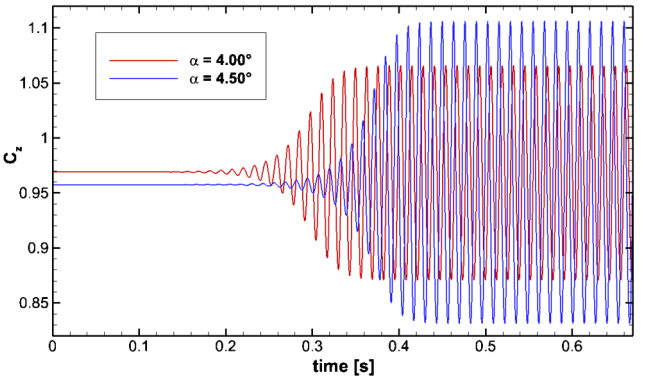

b) Higher angles of attack

Fig. 10 Evolution of lift coefficient in URANS solutions for different angles of attack.

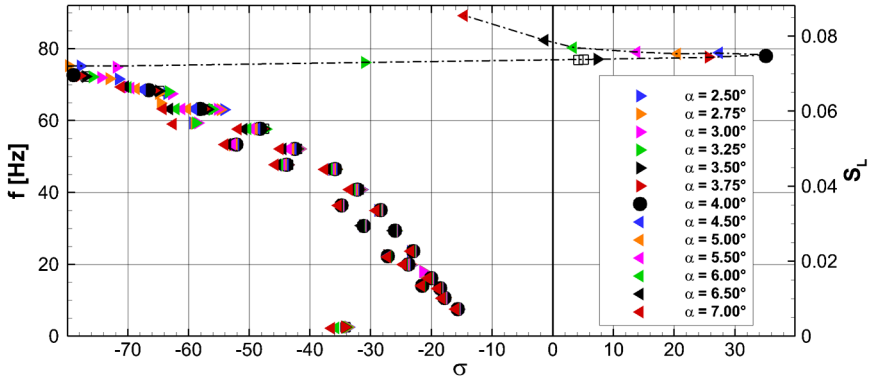

Fig. 11 Eigenvalue spectra for various angles of attack and $M = 0.73$.

authors' knowledge, it has never been documented for the OAT15A profile.

Note that the critical angle for buffet onset obtained here ($\alpha = 3.5$ deg) exactly corresponds to the value found by Deck [10] by means of zonal detached eddy simulation, and it roughly corresponds to the threshold value $\alpha = 3.25$ deg observed in the experiment by Jacquin et al. [28]. However, this value slightly disagrees with the URANS computations by Deck [10], performed with the Spalart–Allmaras turbulence model, where the onset was found to be at $\alpha = 4.0$ deg. The discrepancies between these values could be due to the laminar-turbulent transition of the boundary layer, fixed by a carborundum strip in the experimental case or numerically imposed in the case of Brunet [9] and Deck [10] at $x/c = 0.07$. However, as reported in other configurations [9,11,29], it is known that numerical simulations need a higher angle of attack to reproduce the buffet phenomenon.

IV. Analysis of Unstable Global Modes

We now analyze the stability of the base flows by performing an eigenvalue decomposition of the global Jacobian matrix.

A. Global Modes

We consider the evolution of a small amplitude perturbation $\epsilon \boldsymbol{w}'$ superimposed on the base flow: $\boldsymbol{w} = \bar{\boldsymbol{w}} + \epsilon \boldsymbol{w}'$, with $\epsilon \ll 1$. The equation governing the perturbation is given by the linearization to the first order of the discretized Eq. (2):

$$\frac{\mathrm{d}\boldsymbol{w}'}{\mathrm{d}t} = J\boldsymbol{w}' \tag{4}$$

The Jacobian operator $J \in \mathbb{R}^{N\times N}$ corresponds to the linearization of the discrete Navier–Stokes residual $\mathcal{R}$ around the base flow $\bar{\boldsymbol{w}}$:

$$J_{ij} = \left.\frac{\partial \mathcal{R}_i}{\partial w_j}\right|_{\boldsymbol{w}=\bar{\boldsymbol{w}}} \tag{5}$$

where $\mathcal{R}_i$ designates the ith component of the residual, which is an a priori function of all unknowns w_j in the mesh. The J operator involves spatial derivatives, and it is a sparse matrix. The proposed formalism does not assume homogeneity of the base flow in a given direction, and it corresponds to the biglobal linear-stability analysis, as introduced by [15]. The analysis is two-dimensional (2-D), and we assume that the base flow and fluctuations are homogeneous in the third direction. The stability of a base flow is then determined by scrutinizing the spectrum of the matrix J, and particular solutions of Eq. (4) are sought in the form of normal modes $\boldsymbol{w}' = \hat{\boldsymbol{w}} e^{\lambda t}$. Then, Eq. (4) may be recast into the following eigenvalue problem:

$$J\hat{\boldsymbol{w}} = \lambda \hat{\boldsymbol{w}} \tag{6}$$

The real part of the eigenvalue λ is the growth rate σ. If at least one of the eigenvalues λ exhibits a positive growth rate σ, the base flow $\bar{\boldsymbol{w}}$ is unstable. We refer to unstable flows as oscillators, since the unstable mode will naturally grow and impose its dynamics to the flow. regardless of any external perturbations. Noise amplifiers refer to globally stable flows, in which case an external forcing term is required to maintain unsteadiness.

B. Numerical Strategy

To compute the linearized operator, we follow a strategy based on a finite difference method to obtain $J\boldsymbol{u}$, where $\boldsymbol{u}$ is an arbitrary vector. More precisely, we evaluate the Jacobian matrix by repeated evaluations of the residual function $\mathcal{R}$. The code used to perform a computational fluid dynamics simulation may then be used in a black box manner: assuming that the code generates a valid discrete residual $\mathcal{R}(\boldsymbol{u})$, one may obtain $J\boldsymbol{u}$ with the following first-order approximation:

$$J\boldsymbol{u} = \frac{1}{\epsilon}[\mathcal{R}(\bar{\boldsymbol{w}} + \epsilon \boldsymbol{u}) - \mathcal{R}(\bar{\boldsymbol{w}})] \tag{7}$$

where ε is a small constant. By choosing a series of well-defined vectors $\boldsymbol{u}$, we can compute all the Jacobian coefficients involved in Eq. (5) solely by residual evaluations, which are provided by the numerical code. Moreover, the Jacobian structure is intrinsically linked to the discretization stencil, which we chose to be compact, ensuring the sparsity of the matrix. The procedure is then optimized using a set of vectors $\boldsymbol{u}$ that take into account the stencil discretization of the residual $\mathcal{R}$ in order to compute all the matrix J coefficients with only a few residual evaluations. Note that the shock smoothing proposed by Crouch et al. [30] was not required here, since the linearized equations were obtained by a "discretize-then-linearize" approach rather than a "linearize-then-discretize" approach. More details on the numerical strategy can be found in [31].

The eigenvalue problems in Eq. (6) are solved using Krylov methods combined with a shift-invert strategy (open source library ARPACK [32]), so as to focus on the least-damped eigenvalues. Matrix inversions are carried out in the following with a direct sparse lower–upper (LU) solver for distributed memory machines (MUMPS[§] or SuperLU-dist[¶]). The inverses are quickly obtained. However, this method has very high requirements in terms of memory: typically around 50 times the size of the matrix to be inverted.

C. Results

The eigenvalue spectra for all angles of attack are presented in Fig. 11. It is seen that nearly all eigenvalues are roughly independent of the angle of attack, except one in the frequency range of the buffet phenomenon: a dashed–dotted line in Fig. 11 indicates the trajectory of this eigenvalue as the angle of attack increases. The flow is globally stable for small angles of attack, up to $\alpha = 3.25$ deg. Then, the least stable eigenvalue crosses the real axis between $\alpha = 3.25$ deg and $\alpha = 3.5$ deg: as observed by Crouch et al. [30], the onset of

[§]Data available online at http://graal.ens-lyon.fr/MUMPS/ [retrieved 2014].

[¶]Data available online at http://acts.nersc.gov/superlu/ [retrieved 2014].

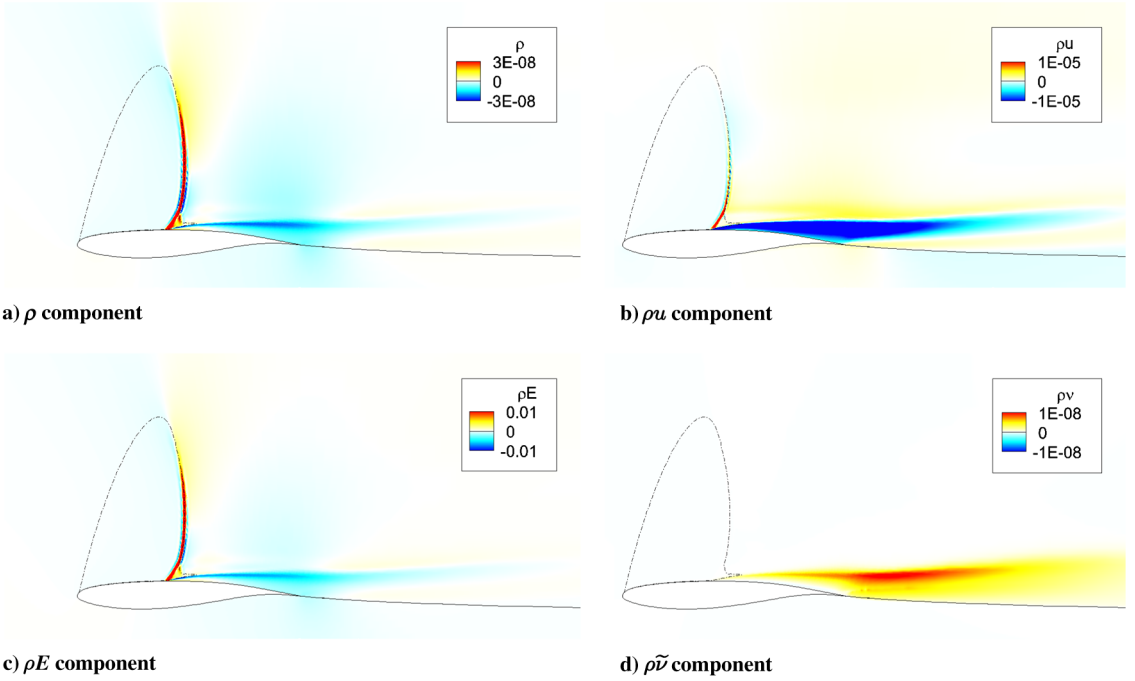

a) ρ component **b) ρu component**

c) ρE component **d) $\rho\tilde{\nu}$ component**

Fig. 12 Unstable global mode for $\alpha = 4.5$ deg and $M = 0.73$. Real parts of different components.

instability is due to a Hopf bifurcation, since the frequency of the mode is nonzero at criticality. A further increase in α results in a strengthening of the instability growth rate, up to $\alpha = 4.0$ deg. Then, the growth rate begins to decrease and we can observe buffet offset after $\alpha = 6.0$ deg.

The physical frequency of the buffet phenomenon resulting from the eigenvalue decomposition near buffet onset at $\alpha = 3.5$ deg is 77 Hz, which is satisfyingly close to the experimental value of 69 Hz found by Jacquin et al. [22] in the same configuration. It is worth saying that a value of exactly 77 Hz was found in the experimental investigation when $M = 0.74$ instead of $M = 0.73$, as in the present study. After buffet onset, the frequency of the unstable mode remains constant up to the most unstable configuration $\alpha = 4.0$ deg, and then it increases up to 80 Hz for $\alpha = 6.0$ deg: the "return to stability" phenomenon goes with a slight increase of the shock-buffet frequency. The angles of attack that define the thresholds of buffet onset and offset compare favorably with the numerical results obtained with the URANS simulation presented in Sec. III. Similarly, the frequency of the unstable modes accurately corresponds to those observed on the saturated limit cycles presented in Sec. III.E. This is a striking result, indicating that the mean flow harmonic and the second-order harmonic generated by nonlinearities remain weak as the amplitude of the unstable global mode increases (see [33]). This is reminiscent of the fact that the mean values of the lift coefficient on the saturated limit cycles correspond to those of the base flows (see Sec. III.E). Such results are not common: for example, in the case of cylinder flow [34], the base-flow and limit-cycle frequencies increasingly diverge as the Reynolds number departs from criticality.

When considering a frozen eddy viscosity approach [31,35], in which case the eddy viscosity is not allowed to fluctuate and is forced to remain constant and equal to the base-flow value, no unstable global modes are found. This observation is in agreement with the study of Crouch et al. [18], who documented the same behavior for the buffet on a NACA airfoil. This also constitutes a striking result, since the frozen eddy viscosity approach usually yields results that are close to those obtained with the linearization of the full operator (see [31] for the case of open-cavity flow).

When considering meshes characterized by finer grid refinement (both the base-flow solution and the eigenvalue problem are solved again), a small shift in the real part of the eigenvalue is observed while the frequency of the mode remains constant: in Fig. 11, the square open symbols show the position of the least-damped eigenvalue at $\alpha = 3.5$ deg, obtained considering different grids. Hence, both the base-flow solutions and the eigenvalue spectra may be considered as spatially converged.

Figure 12 presents the spatial structure of the direct unstable global mode at $\alpha = 4.5$ deg: the mode is most energetic within the shock wave for all the conservative variables, but a nonnegligible contribution is located in the mixing layer. In the horizontal momentum component, the mode is also present in the recirculation bubble. Interestingly, we note that the horizontal momentum component displays values of opposite signs within the shock wave and the separated zone: this indicates that, when the shock moves downstream (positive horizontal momentum perturbations), the bubble contracts (negative horizontal values), and vice versa.

If we look at the turbulence component in Fig. 12, we can notice that the buffet phenomenon is associated to large-scale fluctuations of the eddy viscosity, which propagate in the wake. This is due to the contraction and expansion of the recirculation bubble, caused by the shock displacement.

D. Adjoint Problem

In addition to the direct eigenvalue problem introduced in Eq. (6), we also consider the adjoint problem: we define the adjoint Jacobian matrix $J^\dagger$ such that, for any arbitrary vectors $\boldsymbol{u}$ and $\boldsymbol{v}$, we have

$$\langle \boldsymbol{u}, J\boldsymbol{v}\rangle_Q = \langle J^\dagger \boldsymbol{u}, \boldsymbol{v}\rangle_Q \tag{8}$$

The scalar product $\langle\cdot,\cdot\rangle_Q$ is a discrete inner product in $\mathbb{C}^N$ based on a positive definite Hermitian matrix Q, such that

$$\langle \boldsymbol{u}, \boldsymbol{v}\rangle|_Q = \boldsymbol{u}^* Q \boldsymbol{v} \tag{9}$$

where $*$ denotes the conjugate transpose. We choose Q so that $\langle \boldsymbol{u}, \boldsymbol{u}\rangle|_Q$ represents the square of the function 2-norm. With a finite volume approach, Q is then a real diagonal matrix for which the terms Q_i correspond to the volume Ω_i of each cell i. The solutions of the adjoint eigenproblem $\tilde{\boldsymbol{w}}$ are given by

$$J^\dagger \tilde{\boldsymbol{w}} = \lambda^* \tilde{\boldsymbol{w}} \tag{10}$$

where the quantity $\tilde{\boldsymbol{w}}$ is called the adjoint global mode, associated to the direct global mode $\hat{\boldsymbol{w}}$ [14]. The convection operator present in the

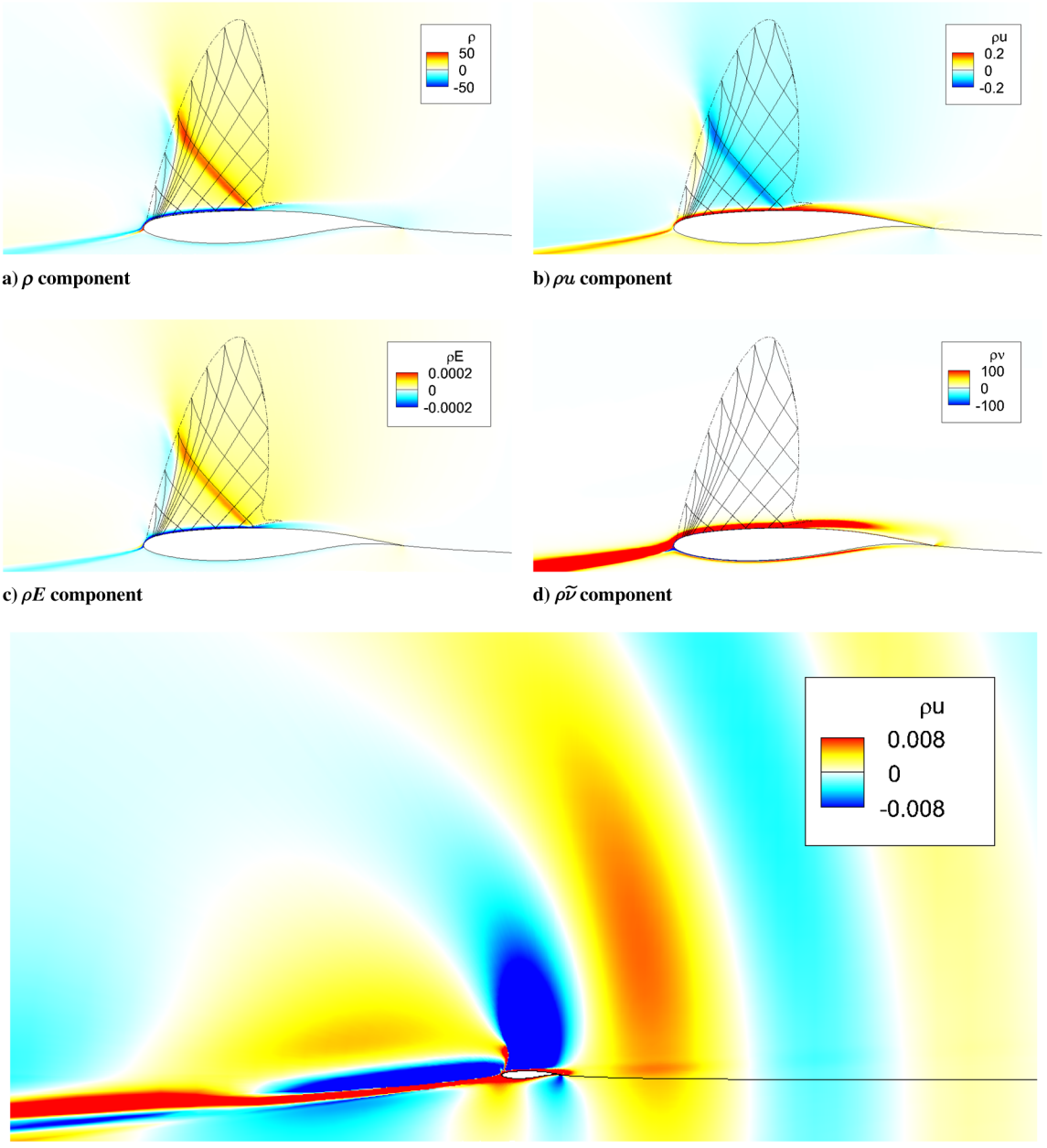

a) ρ component

b) ρu component

c) ρE component

d) $\rho\tilde{\nu}$ component

e) ρu component, large domain

Fig. 13 Unstable adjoint mode for $\alpha = 4.5$ deg and $M = 0.73$. Real parts of different components. The sonic and characteristic lines in the supersonic region are depicted with dashed–dotted and solid lines.

governing equations yields a strongly nonnormal Jacobian J, so that perturbations propagate downstream in the direct global mode and upstream in the adjoint global mode [36]. The adjoint global mode indicates the most sensitive region to manipulate the buffet phenomenon: more precisely, it is the optimal region in space where a harmonic forcing has strongest effect on the dynamics of the unstable global mode, in order to either suppress/strengthen the oscillation amplitudes on the saturated limit cycle or modify its frequency [21].

The adjoint global mode is depicted in Fig. 13 for the configuration corresponding to $\alpha = 4.5$ deg. The most sensitive regions are localized mostly on the suction side of the profile, in the boundary layer upstream of the shock foot and in the recirculation bubble. The adjoint global mode in the supersonic flow region has a triangular shape, for which the edges follow the boundary layer, the upwind part of the sonic line, and an oblique line impinging on the profile exactly where the boundary layer separates.

To investigate the nature of this line, we consider the theory of characteristics [37]: by recasting the hyperbolic equations governing the compressible flow in characteristic form, we obtain typical lines, called the characteristic lines, along which information propagates in the supersonic region. The angle of those lines with respect to the base-flow velocity direction is given by

$$\gamma = \pm\tan^{-1}\sqrt{\frac{1}{M_l^2 - 1}} \tag{11}$$

where M_l is the local Mach number. Figures 13a–13d show the superposition of the adjoint global mode with the left and right characteristic lines, associated to the negative and positive signs in Eq. (11), respectively. In particular, the right characteristic lines run from the top left to the bottom right of the figure, whereas the left characteristic lines run from the bottom left to the top right.

The oblique part of the adjoint global mode follows exactly the right characteristic line that impacts on the shock foot, where the recirculation bubble begins. This feature can be interpreted as

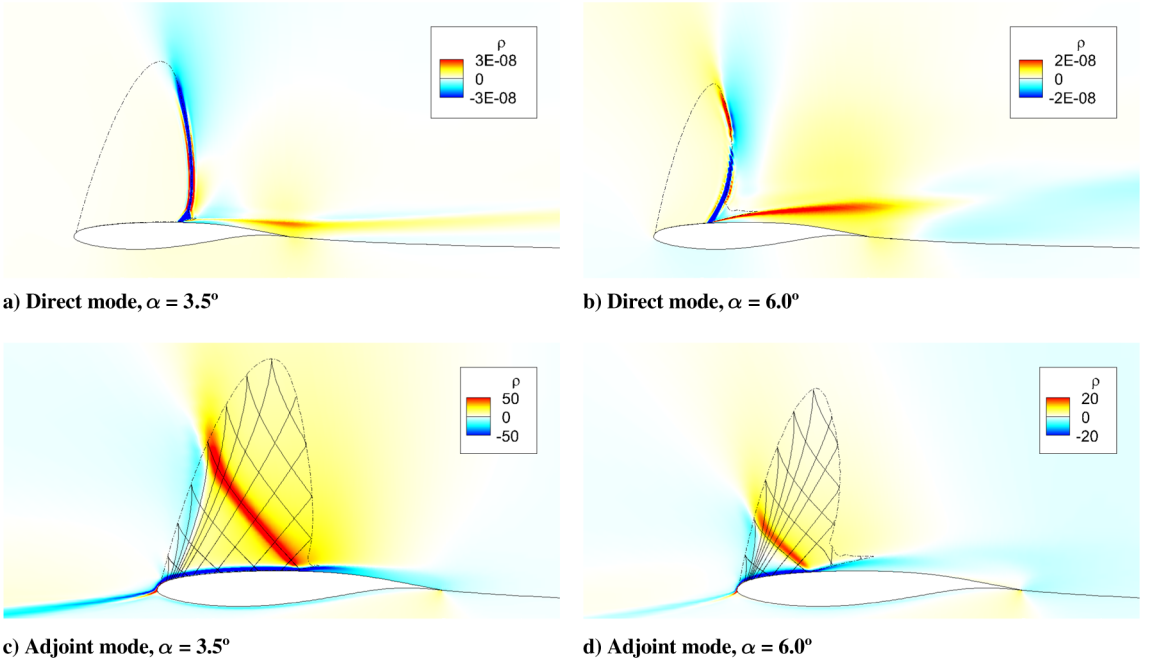

a) Direct mode, $\alpha = 3.5^o$ b) Direct mode, $\alpha = 6.0^o$

c) Adjoint mode, $\alpha = 3.5^o$ d) Adjoint mode, $\alpha = 6.0^o$

Fig. 14 Direct and adjoint unstable global modes near buffet onset and offset. Real parts of density components.

follows: the separation point has fundamental importance in the dynamics of the flow, and a modification of its position can influence the whole dynamics. The adjoint global mode indicates the zone where the flow presents high receptivity to external forcing. As in a supersonic flow, information travels along characteristic lines, and only the supersonic region that is connected to the separation point through a characteristic line can influence this separation point.

We can see that the adjoint global mode follows the left characteristic lines only in the upwind part of the supersonic zone. Yet, it is seen that its amplitude in this region is quite low. This may be explained as follows. The left characteristic lines in this region reflect on the sonic line and propagate along the right characteristic lines that hit the separation point. The difference in amplitude suggests that pressure disturbances that propagate along the left characteristic lines from the profile to the sonic line have less impact on the buffet phenomenon than the same disturbances localized directly on the right characteristic lines and that travel toward and hit the separation point. This may be understood from the fact that the reflection of the disturbances on the sonic line involves some losses. Note, finally, that these left characteristic lines can be seen in the schlieren image of Fig. 2 by the bright curved line close to the compression wave generated by the carborundum strip. This indicates that these specific lines may have some importance in the physics of the buffet phenomenon. Agostini et al. [38] have recently performed large eddy simulation computations of an oblique shock at Mach number $M = 2.3$ reflecting on a turbulent boundary layer. Using two-point correlations, they showed how vortical structures in the mixing layer generate pressure fluctuations that propagate along the characteristic lines of the expansion fan. This clearly indicates how pressure disturbances can travel along these characteristics.

In Fig. 13e, we can also observe the spatial structure of the adjoint global mode far away from the profile: the adjoint mode is located in the part of the incoming flow that will be convected into the boundary layers around the profile, showing that disturbances upstream of the aerofoil may have an influence on the buffeting phenomenon. Finally, it is seen that excitations downstream of the aerofoil may also (weakly) perturb the phenomenon due to the fact that acoustic waves propagate upstream in the freestream subsonic flow.

Figure 14 shows the direct and adjoint global modes for the configurations corresponding to buffet onset and offset. Even if the base flow presents some differences in terms of shock position, separation point location, and size of the recirculation bubble, the location and spatial structure of the direct and adjoint global modes remain roughly unchanged.

Following Sipp [21], the spatial structure of the adjoint global mode indicates the optimal harmonic forcing structure to modify and shift the natural nonlinear frequency of the flow (lock-on phenomenon). Harmonic forcings may be based either on application of forces, energy sources/sinks (heating/cooling), or eddy viscosity sources/sinks (vortex generators). The preferred regions consist of the boundary layer upstream of the shock foot, the recirculation region, and the right characteristic line impinging the shock foot.

Concerning the spatial structure of the adjoint global modes, Figs. 13 and 14 show that the adjoint variables are continuous with zero gradient across the shock wave. This feature has been demonstrated in quasi-one-dimensional Euler equations [39] using a theoretical approach that relies on the derivation of a closed-form solution of the adjoint equations. In the same paper, it is shown how a change in sign in either of the hyperbolic characteristic lines is responsible for a $\log(x)$ singularity at the sonic point. However, for two-dimensional configurations, as is the case here, considering the influence region of points in the neighborhood of the sonic line, it may be shown that such singularities no longer exist [40].

E. Eigenvalue Sensitivity and Passive Control

Passive control may be studied by considering the sensitivity of the unstable eigenvalue with respect to the introduction of steady source terms in the Navier–Stokes equations. Such an analysis highlights regions of the flow where the introduction of a local control device, which acts as a steady forcing at the base flow level, yields the strongest shift in either the amplification rate or the frequency of the global mode [20,41,42].

The eigenvalue λ is a function of the Jacobian J, which is a function of the base flow $\bar{\boldsymbol{w}}$, which is itself a function of the steady forcing $\boldsymbol{f}$. The eigenvalue λ is therefore a function of the steady forcing $\boldsymbol{f}$. Therefore, a first-order Taylor expansion of this function leads to

$$\delta\lambda = \langle \nabla_f \lambda, \delta \boldsymbol{f} \rangle_Q \tag{12}$$

where $\nabla_f \lambda$ is the gradient of the eigenvalue with respect to the steady forcing $\boldsymbol{f}$. Mettot et al. [31] showed that, in a discrete framework, $\nabla_f \lambda$ may be related to the direct mode $\hat{\boldsymbol{w}}$ and adjoint mode $\tilde{\boldsymbol{w}}$ through

$$\nabla_f \lambda = -J^{\dagger -1} H^{\dagger} \tilde{\boldsymbol{w}} \tag{13}$$

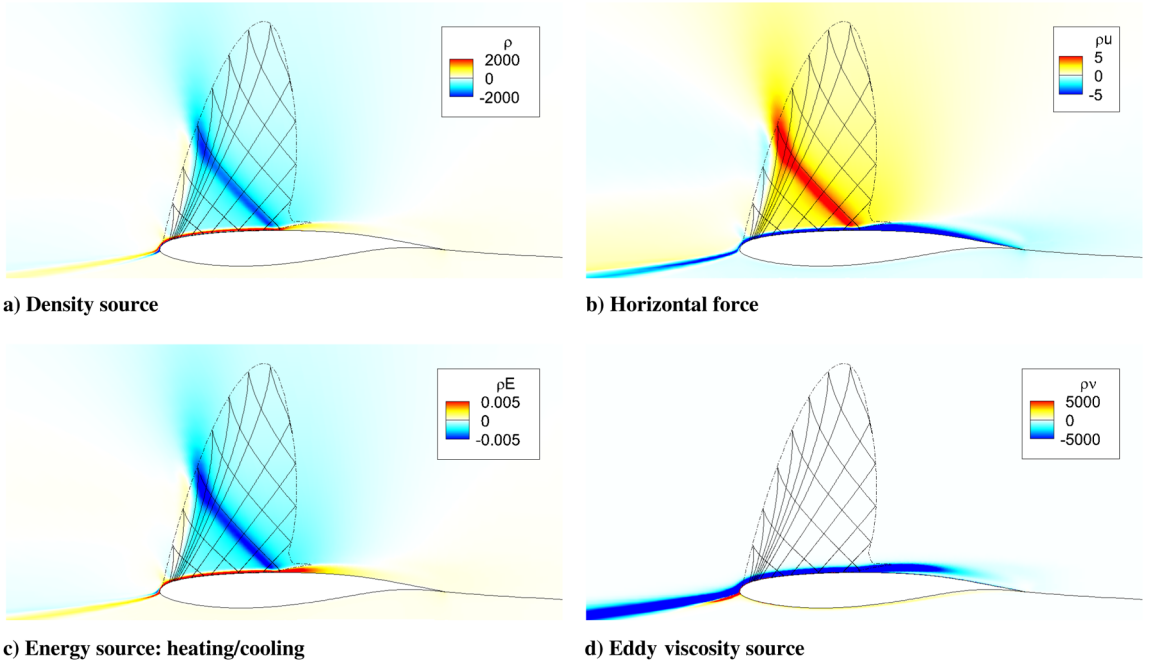

a) Density source b) Horizontal force

c) Energy source: heating/cooling d) Eddy viscosity source

Fig. 15 Sensitivity of the growth rate $\nabla_f \sigma$ to a steady forcing, for $\alpha = 4.5$ deg.

where $H = \partial[J(\bar{\boldsymbol{w}})\hat{\boldsymbol{w}}]/\partial\bar{\boldsymbol{w}}$ is a linear operator related to the Hessian of the governing Navier–Stokes equations. The matrix H is sparse and verifies for an arbitrary vector $\boldsymbol{u}$:

$$H\boldsymbol{u} = \frac{1}{\epsilon_1\epsilon_2}[\mathcal{R}(\bar{\boldsymbol{w}} + \epsilon_1\hat{\boldsymbol{w}} + \epsilon_2\boldsymbol{u}) - \mathcal{R}(\bar{\boldsymbol{w}} + \epsilon_1\hat{\boldsymbol{w}}) - \mathcal{R}(\bar{\boldsymbol{w}} + \epsilon_2\boldsymbol{u}) + \mathcal{R}(\bar{\boldsymbol{w}})] \tag{14}$$

Here, ϵ_1 and ϵ_2 are small parameters. All nonzero coefficients of H may then be explicitly computed from residual evaluations using the previous equation. Note that the optimal set of vectors used for the Jacobian computation can also be used to compute the matrix H.

In the present work, we focus on control objectives that stabilize or strengthen the instability. We therefore only analyze the real part of the gradient fields, which are plotted in Fig. 15. If we focus on the streamwise momentum source shown in Fig. 15b, we can observe that a streamwise force in the upstream boundary layer or in the recirculation bubble will have a stabilizing effect on the unstable mode. Action in the boundary layer can be interpreted as an energizing effect of the boundary layer that becomes less prone to separation, whereas action in the recirculation bubble directly shrinks the separated zone. Considering Fig. 15c, the energy component indicates that a steady cooling of the boundary layer will also stabilize the unstable global mode. Finally, considering the turbulence variable in Fig. 15d, a negative value in the sensitivity map in the boundary layer indicates that an increase of the eddy viscosity in the boundary layer (caused for example by a mechanical vortex generator) will have a stabilizing effect on the buffet mode. Again, this may be interpreted by the fact that the size of the separated region will decrease in this case.

V. Analysis of Pseudoresonances

The flowfield may exhibit strong responses for particular forcings and frequencies due to the nonnormality of the linearized Navier–Stokes operator [14,17,43]. We here analyze the receptivity of the flow to external forcings, which are always present in the upstream flow (turbulence, acoustic perturbations, etc.). More precisely, for each frequency, we will extract optimal forcings that lead to the largest responses: the optimal responses. Such an analysis indicates the favored frequencies of the flow: in particular, an analysis of the structure of the optimal forcings/responses may highlight the respective role of the shock, the mixing layer, or the recirculation bubble within an amplification process. A similar approach has already been used to describe pseudoresonances in a channel-flow configuration [44], turbulent pipe flow [45], Blasius boundary layer [46], and jets [47].

The numerical simulations of Sec. III and the global-mode decomposition of Sec. IV indicate that the flow presents self-sustained low-frequency oscillations when the angle of attack is between $\alpha = 3.5$ deg and $\alpha = 6.0$ deg. In those cases, the dynamics of the flow is dominated by the unstable large-scale perturbation, described by the unstable global mode. However, the flow may additionally exhibit fluctuations that are driven by existing external perturbations, such as noise or freestream turbulence. In the case of angles of attack below buffet onset and above buffet offset, pseudoresonances are the only cause of large-scale low-frequency perturbations. Recall that high-frequency small-scale perturbations may not be captured by an unsteady RANS approach, since such perturbations are already accounted for by the turbulence model.

A. Optimal Gains/Forcings/Responses

We consider the response of the flow to small-amplitude external momentum forcings $\epsilon\boldsymbol{f}'$:

$$\frac{\mathrm{d}\boldsymbol{w}}{\mathrm{d}t} = \mathcal{R}(\boldsymbol{w}) + \epsilon P\boldsymbol{f}' \tag{15}$$

where P is a prolongation matrix, which adds zero components to a vector containing solely horizontal and vertical momentum forcings so as to obtain a full vector with density–momentum–energy and eddy viscosity components. Again, we look for the solutions under the form $\boldsymbol{w} = \bar{\boldsymbol{w}} + \epsilon\boldsymbol{w}'$. At first order, we obtain

$$\frac{\mathrm{d}\boldsymbol{w}'}{\mathrm{d}t} = J\boldsymbol{w}' + \boldsymbol{f}' \tag{16}$$

We consider, at a given real frequency ω, a forcing and a response under the forms $\boldsymbol{f}' = \hat{\boldsymbol{f}}(x,y)e^{i\omega t}$ and $\boldsymbol{w}' = \hat{\boldsymbol{w}}(x,y)e^{i\omega t}$. Simplifying and rearranging the equation for $\hat{\boldsymbol{w}}$ yields

$$\hat{\boldsymbol{w}} = R\hat{\boldsymbol{f}} \tag{17}$$

where $R(\omega) = (i\omega\boldsymbol{I} - J)^{-1}P$ is the global resolvent matrix.

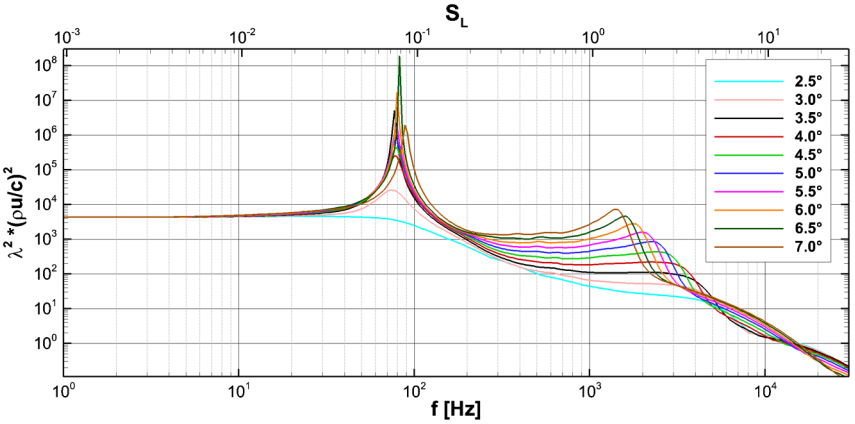

Fig. 16 Gain function for different angles of attack.

The relation in Eq. (17) gives access, for a given frequency, to the harmonic response $\hat{\boldsymbol{w}}$ of the system when forced with a harmonic forcing of a given spatial form $\hat{\boldsymbol{f}}$. We now introduce the gain G, which is the function of the external forcing $\hat{\boldsymbol{f}}$, which is defined for every frequency as the ratio between the kinetic energy of the response and the squared L2 function norm of the momentum forcing itself:

$$G(\hat{\boldsymbol{f}}) = \frac{\langle \hat{\boldsymbol{w}}, \hat{\boldsymbol{w}} \rangle_{Q_e}}{\langle \hat{\boldsymbol{f}}, \hat{\boldsymbol{f}} \rangle_{Q}} \tag{18}$$

For the forcing, the scalar product is the same as the one used in Eq. (9), except that only the momentum components are considered. For the flow response, as we would like the numerator of gain function (18) to be the kinetic energy

$$E = \int (u^2 + v^2)\, \mathrm{d}x\, \mathrm{d}y$$

of the response $\hat{\boldsymbol{w}}$, we define a pseudoscalar product $\langle \cdot, \cdot \rangle_{Q_e}$ such that

$$\langle \boldsymbol{w}, \boldsymbol{w} \rangle|_{Q_e} = \boldsymbol{w}^* Q_e \boldsymbol{w} = E \tag{19}$$

Among all the possible forcings, we are looking for the one that causes the strongest response in the flow, and thus the forcing that maximizes the gain function, which is called the optimal forcing. Introducing Eq. (17) into Eq. (18), we obtain

$$G_{\max}(\hat{\boldsymbol{f}}) = \sup_{\hat{f}} \frac{\langle R\hat{\boldsymbol{f}}, R\hat{\boldsymbol{f}} \rangle_{Q_e}}{\langle \hat{\boldsymbol{f}}, \hat{\boldsymbol{f}} \rangle_{Q}} = \sup_{\hat{f}} \frac{\langle R^\dagger R\hat{\boldsymbol{f}}, \hat{\boldsymbol{f}} \rangle_{Q}}{\langle \hat{\boldsymbol{f}}, \hat{\boldsymbol{f}} \rangle_{Q}} \tag{20}$$

where $R^\dagger$ is the adjoint operator such that $\langle \hat{\boldsymbol{a}}, R\hat{\boldsymbol{b}} \rangle_{Q_e} = \langle R^\dagger \hat{\boldsymbol{a}}, \hat{\boldsymbol{b}} \rangle_{Q}$ for all $\hat{\boldsymbol{a}}$ and $\hat{\boldsymbol{b}}$. For each frequency ω, this optimization problem can be solved by performing a singular-value decomposition of the resolvent R or by determining the largest eigenvalue μ^2, also called the optimal gain, of the following eigenproblem:

$$R^\dagger R\hat{\boldsymbol{f}} = \mu^2 \hat{\boldsymbol{f}} \tag{21}$$

The structure $\hat{\boldsymbol{f}}$ is called the optimal forcing, whereas the associated optimal response $\hat{\boldsymbol{w}}$ can be obtained by solving Eq. (17).

The global resolvent is well defined as long as the matrix $(i\omega \boldsymbol{I} - J)$ is not singular. This condition is fulfilled for a given frequency ω, if there is no eigenvalue of the Jacobian matrix J displaying a real part equal to zero and an imaginary part equal to ω. If this is the case, then the optimal gain tends to infinity, whereas the optimal forcing and response tend to the marginal adjoint and direct global modes of frequency ω.

From a numerical point of view, to compute the optimal gains/forcings/responses, we again use Krylov methods (ARPACK in regular mode instead of shift-invert mode) and direct LU solvers (MUMPS) to evaluate the matrix inverses involved in R and $R^\dagger$.

B. Results

The optimal gains μ^2, nondimensionalized by $\rho_\infty^2 U_\infty^2 / c^2$, are presented in Fig. 16 as a function of frequency, for different angles of attack. The overall shape of the gain function corresponds roughly to a low-pass filter behavior: for all angles of attack, the very first part of the gain function is a straight horizontal line, whereas a strong decrease of the gains is observed at high frequencies of $f > 10$ kHz. Such a behavior is reminiscent of the results by Plotkin [48] and Touber and Sandham [49], who argued that the shock exhibits such a behavior.

Considering the low-frequency dynamics of $f \leq 200$ Hz, the curves present strong peaks around $\alpha = 3.5$ deg and $\alpha = 6.0$ deg: in those configurations, the buffet global mode is closest to the imaginary axis and the optimal gain tends to infinity, as discussed before. The highest gains correspond to the frequencies characteristic of the buffet modes. We observe a slight increase of the frequency of the optimal gain peak, in accordance with the increase of the global mode's frequency presented in Sec. IV.C.

Considering the optimal gains at medium frequencies (200 Hz $< f <$ 10 kHz) in Fig. 16, we can notice a rise of the gains as the angle of attack increases. The eigenvalue spectra presented in Sec. IV did not reveal any global mode approaching marginality in this frequency range. Hence, the bumps in the optimal gain curves observed around $f \approx 2$–3 kHz correspond to pseudoresonance mechanisms.

In the following, we will only discuss the spatial structures of the optimal forcings/responses for the medium-frequency peaks and not for the low-frequency peaks, since for the latter peaks, the optimal forcings/responses are very close to the adjoint-direct global modes presented before. Figure 17 presents the optimal forcings for the medium-frequency peak frequencies for four different configurations. Those frequencies are $f = 4000$ Hz for $\alpha = 2.5$ deg, $f = 3000$ Hz for $\alpha = 4.0$ deg, $f = 2000$ Hz for $\alpha = 5.5$ deg, and $f = 1400$ Hz for $\alpha = 7.0$ deg. The optimal forcings are located near the wall on the whole suction side surface for low angles of attack, and upstream of the shock location for higher α, with a maximum value at the shock foot. In the supersonic zone, the forcing does not exactly follow the right characteristic lines that end at the separation point. Also, it is seen that the forcings display rather small-scale structures, in accordance with the fact that the considered frequencies are an order of magnitude higher than in the case of the unstable global modes. Note that, according to Sipp and Marquet [50], it could be interesting to exploit the strong receptivity of the flow at these medium frequencies to manipulate and stabilize the unstable global mode at low frequency: one may then show that the best excitation structure corresponds to the optimal forcing, which generates the most energetic response.

The optimal responses associated to those medium-frequency forcings are presented in Fig. 18. They indicate that Kelvin–Helmholtz-type instabilities are at play, with two zones affected by

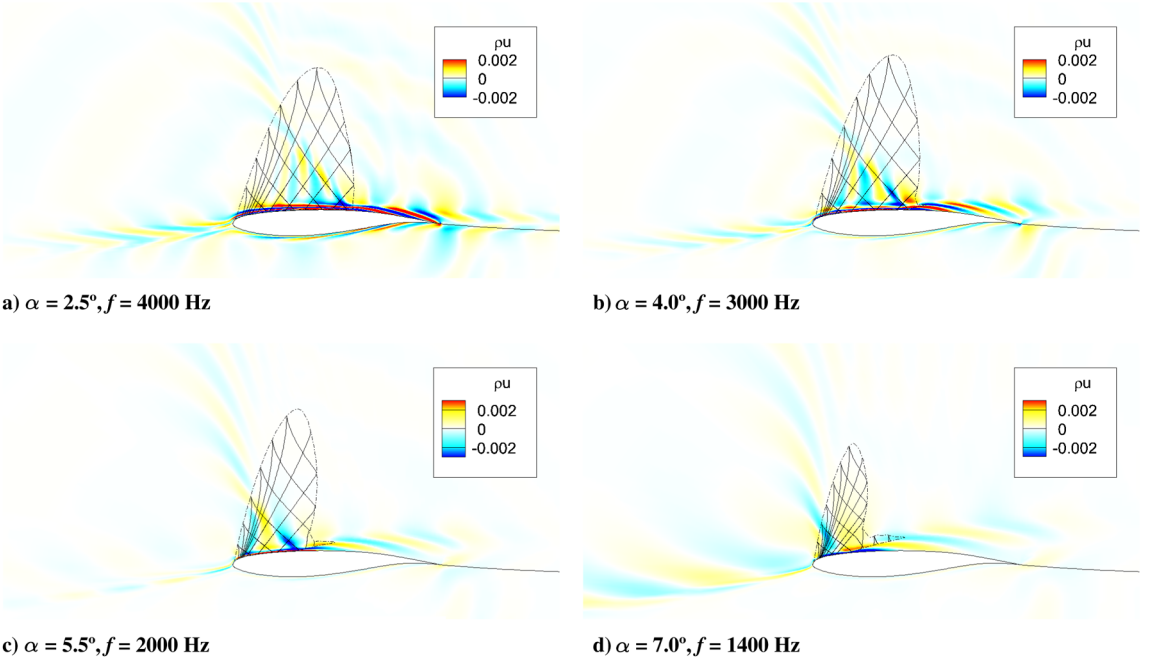

a) $\alpha = 2.5^{\circ}, f = 4000$ Hz b) $\alpha = 4.0^{\circ}, f = 3000$ Hz

c) $\alpha = 5.5^{\circ}, f = 2000$ Hz d) $\alpha = 7.0^{\circ}, f = 1400$ Hz

Fig. 17 Horizontal force component of optimal forcings for medium-frequency unsteadiness, for various angles of attack and $M = 0.73$.

these medium-frequency motions: the mixing layer caused by the separated region and the mixing layer after the trailing edge.

Comparing the optimal responses in Fig. 18, one can notice that the amplitudes grow as the angle of attack increases and that the contribution of the separated zone is roughly the same as the contribution due to the trailing edge: the peak in the gain function indicates that medium-frequency instabilities are the most energetic for the frequency that can trigger, at the same time, both the mixing-layer unsteadiness at the shock foot and on the trailing edge.

The evolution of the gain function in Fig. 16 indicates that the optimal Kelvin–Helmholtz instability frequency becomes smaller as α is increased. This behavior may be due to the fact that this unsteadiness depends on the mixing layer thickness: the higher the angle of attack, the larger the separated zone, and thus the smaller the frequency. However, the medium-frequency unsteadiness is broadband, indicating that, in the flow, Kelvin–Helmholtz-type instabilities are present in the range of 1–4 kHz, contrary to the buffet unsteadiness, which is characterized by a very narrow peak in the frequency spectrum.

VI. Conclusions

This paper focused on the unsteady dynamics of the transonic interaction between a shock and a boundary layer over an OAT15A profile. The experimental investigation performed by Jacquin et al. [28] is considered as a reference experimental case and is used to compare the results. Two-dimensional numerical simulations are shown to reproduce the periodic motions of the shock wave, known as the buffet phenomenon: the simulations satisfactorily predict the unsteady behavior of the interaction, and both the frequency of the shock motions as well as the critical angle of attack that characterize the buffet onset are in fair agreement with the experimental investigation. Buffet offset is also observed when the angle of attack

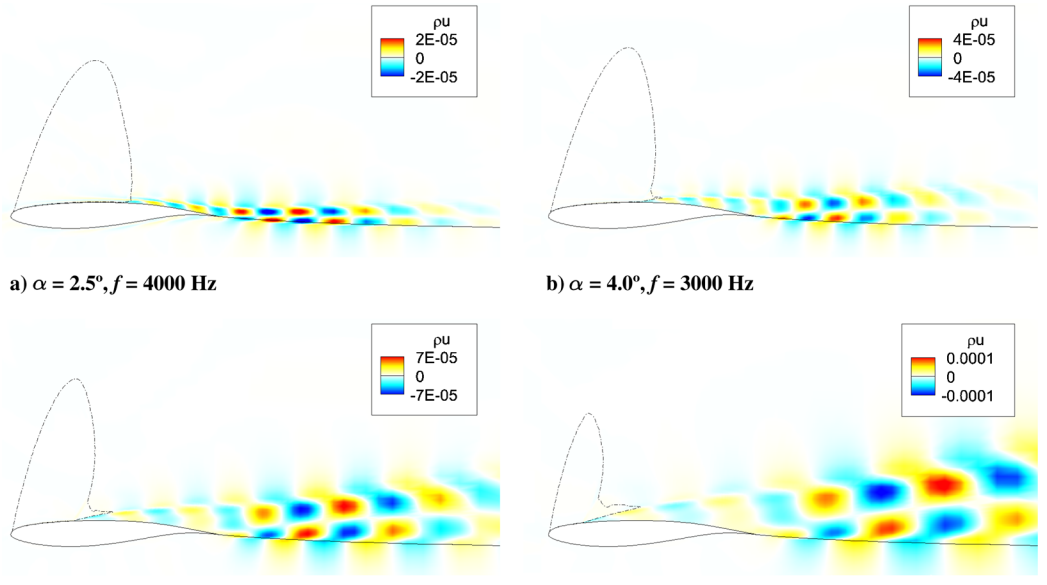

a) $\alpha = 2.5^{\circ}, f = 4000$ Hz b) $\alpha = 4.0^{\circ}, f = 3000$ Hz

c) $\alpha = 5.5^{\circ}, f = 2000$ Hz d) $\alpha = 7.0^{\circ}, f = 1400$ Hz

Fig. 18 Horizontal momentum component of optimal response for medium-frequency unsteadiness, for various angles of attack and $M = 0.73$.

exceeds $\alpha = 6.0$ deg. The results recover and extend the numerical results obtained in previous studies [9,10].

The steady-state solutions of the RANS equations (the base flows) are then considered for a stability analysis. In agreement with [18], an eigenvalue decomposition of the Jacobian matrix indicates that the buffet phenomenon is linked to a global instability of the flow. The angle of attack that defines the threshold of the unsteady shock motions is in agreement with the numerical simulation, and the buffet offset is accompanied by a small rise in the buffet frequency. The direct global mode compares favorably with the stability analysis performed by Crouch et al. [18], whereas the adjoint global mode, for which the spatial distribution follows the characteristic lines in the supersonic region of the flow, can be considered to analyze the receptivity of the flow. Also, the sensitivity gradients showed that a streamwise momentum force in the boundary layer or in the recirculation region, a cooling of the flow, or an increase of the eddy viscosity in the attached boundary layer manage to stabilize the unstable eigenvalue. Such results are in agreement with experimental investigations, which showed that vortex generators in the upstream boundary layer were efficient means to suppress the buffeting phenomenon.

The eigenvalue decomposition of the Jacobian matrix indicates that the shock buffet is the only global instability present in the interaction. However, convective instabilities can arise when the flow is subject to external forcing, such as turbulence or acoustic perturbations existing in the freestream. A singular-value decomposition of the global resolvent is performed, and the gain function shows that the interaction behaves roughly as a low-pass filter: constant gains are obtained at very low frequencies, whereas a strong decrease of the gains is observed for high frequencies ($f > 10$ kHz). Concerning medium-frequency motions, the global-resolvent analysis indicates that medium-scale unsteadiness can arise from the separated zone. The medium-frequency motions are present, both in the mixing-layer above the separated region as well as in the mixing layer at the trailing edge of the profile. This unsteadiness is shown to be broadband and not related to the presence of a stable global mode that approaches marginality at medium frequencies. Moreover, the intensity of the gains increases with the interaction strength, whereas the peak frequency decreases as the angle of attack is increased.

From a physical point of view, the buffeting phenomenon displays some striking features that will be summed up here: the frequency of the global modes mainly depends on the Mach number and not on the angle of attack. This shows that the size of the separation region is not a key parameter of the phenomenon. Also, when time marching the unsteady RANS equations, the mean lift coefficient remains equal to the lift coefficient of the base flow: this indicates that the mean flow harmonic generated by the buffeting mode is weak. Also, it has been shown that the frequency of the flow on the saturated limit cycle remains equal to the frequency of the linear global mode: this indicates again that the mean flow harmonic is weak, but also that the second harmonic is weak [33]. These observations are in stark contrast with respect to more traditional flows undergoing a Hopf bifurcation, such as the cylinder flow or the open-cavity flow [33]. Finally, note that, in the present case, a frozen eddy viscosity approach does not manage to capture the unstable global modes: to the authors' knowledge, this is the sole example of instability where a frozen eddy viscosity approach does not yield approximately the same results as a full approach [31,35].

Acknowledgments

The authors would like to acknowledge the financial support of the French Agence Nationale de la Recherche through the Décollemnts Compressibles et Oscillations Auto-Induites program, project number ANR-10-BLANC-914. We are also grateful to Sébastien Deck, from the ONERA–The French Aerospace Lab Département d'aérodynamique appliquée (Applied Aerodynamics Department) department, for his helpful advices on the numerical simulations.

References

[1] Dolling, D. S., "Fifty Years of Shock-Wave/Boundary-Layer Interaction Research: What Next?," *AIAA Journal*, Vol. 39, No. 8, 2001, pp. 1517–1531. doi:10.2514/2.1476

[2] Délery, J., and Marvin, J. G., "Shock-Wave Boundary Layer Interactions," *AGARDograph*, AGARD-AD-280, 1986.

[3] Délery, J., "Flow Physics Involved in Shock Wave/Boundary Layer Interaction Control," *Iutam Symposium on Mechanics of Passive and Active Flow Control*, Springer, New York, 2000, pp. 15–22.

[4] Pearcey, H. H., "A Method for the Prediction of the Onset of Buffeting and Other Separation Effects from Wind Tunnel Tests on Rigid Models," AGARD TR-223, 1958.

[5] McDevitt, J. B., and Okuno, A. F., "Static and Dynamic Pressure Measurements on a NACA 0012 Airfoil in the Ames High Reynolds Number Facility," NASA TP-2485, 1985.

[6] Lee, B. H. K., "Oscillatory Shock Motion Caused by Transonic Shock Boundary-Layer Interaction," *AIAA Journal*, Vol. 28, No. 5, 1990, pp. 942–944. doi:10.2514/3.25144

[7] Lee, B. H. K., "Self-Sustained Shock Oscillations on Airfoils at Transonic Speeds," *Progress in Aerospace Sciences*, Vol. 37, No. 2, 2001, pp. 147–196. doi:10.1016/S0376-0421(01)00003-3

[8] Barakos, G., and Drikakis, D., "Numerical Simulation of Transonic Buffet Flows Using Various Turbulence Closures," *International Journal of Heat and Fluid Flow*, Vol. 21, No. 5, 2000, pp. 620–626. doi:10.1016/S0142-727X(00)00053-9

[9] Brunet, V., "Computational Study of Buffet Phenomenon with Unsteady RANS Equations," AIAA Paper 2003-3679, 2003.

[10] Deck, S., "Numerical Simulation of Transonic Buffet over the OAT15A Airfoil," *AIAA Journal*, Vol. 43, No. 7, 2005, pp. 1556–1566. doi:10.2514/1.9885

[11] Thiery, M., and Coustols, E., "Numerical Prediction of Shock Induced Oscillations over a 2-D Airfoil: Influence of Turbulence Modelling and Test Section Walls," *International Journal of Heat and Fluid Flow*, Vol. 27, No. 4, 2006, pp. 661–670. doi:10.1016/j.ijheatfluidflow.2006.02.013

[12] Dussauge, J. P., Dupont, P., and Debiève, J. F., "Unsteadiness in Shock Wave Boundary Layer Interactions with Separation," *Aerospace Science and Technology*, Vol. 10, No. 2, 2006, pp. 85–91. doi:10.1016/j.ast.2005.09.006

[13] Erengil, M. E., and Dolling, D. S., "Unsteady Wave Structure Near Separation in a Mach 5 Compression Ramp Interaction," *AIAA Journal*, Vol. 29, No. 5, 1991, pp. 728–735. doi:10.2514/3.10647

[14] Sipp, D., Marquet, O., Meliga, P., and Barbagallo, A., "Dynamics and Control of Global Instabilities in Open-Flows: a Linearized Approach," *Applied Mechanics Reviews*, Vol. 63, No. 3, 2010, Paper 30801. doi:10.1115/1.4001478

[15] Theofilis, V., "Global Linear Instability," *Annual Review of Fluid Mechanics*, Vol. 43, Jan. 2011, pp. 319–352. doi:10.1146/annurev-fluid-122109-160705

[16] Batchelor, G., Moffatt, H., and Worster, M., *Perspectives in Fluid Dynamics*, Cambridge Univ. Press, New York, 2000, pp. 159–229.

[17] Trefethen, L., Trefethen, A., Reddy, S., and Driscoll, T., "Hydrodynamic Stability Without Eigenvalues," *Science*, Vol. 261, No. 5121, 1993, pp. 578–584. doi:10.1126/science.261.5121.578

[18] Crouch, J. D., Garbaruk, A., Magidov, D., and Travin, A., "Origin of Transonic Buffet on Aerofoils," *Journal of Fluid Mechanics*, Vol. 628, No. 1, 2009, pp. 357–369. doi:10.1017/S0022112009006673

[19] Jackson, C. P., "A Finite-Element Study of the Onset of Vortex Shedding in Flow Past Variously Shaped Bodies," *Journal of Fluid Mechanics*, Vol. 182, No. 1, 1987, pp. 23–45. doi:10.1017/S0022112087002234

[20] Marquet, O., Sipp, D., and Jacquin, L., "Sensitivity Analysis and Passive Control of Cylinder Flow," *Journal of Fluid Mechanics*, Vol. 615, Nov. 2008, p. 221. doi:10.1017/S0022112008003662

[21] Sipp, D., "Open-Loop Control of Cavity Oscillations with Harmonic Forcings," *Journal of Fluid Mechanics*, Vol. 708, Oct. 2012, pp. 439–468. doi:10.1017/jfm.2012.329

[22] Jacquin, L., Molton, P., Deck, S., Maury, B., and Soulevant, D., "Experimental Study of Shock Oscillation over a Transonic Supercritical Profile," *AIAA Journal*, Vol. 47, No. 9, 2009, pp. 1985–1994. doi:10.2514/1.30190

[23] Cambier, L., Heib, S., and Plot, S., "The ONERA elsA CFD Software: Input from Research and Feedback from Industry," *Mechanics and Industry*, Vol. 14, No. 1, 2013, pp. 159–174. doi:10.1051/meca/2013056

[24] Spalart, P. R., and Allmaras, S. R., "A One-Equation Turbulence Model for Aerodynamic Flows," AIAA Paper 1992-0439, 1992.

[25] Mary, I., Sagaut, P., and Deville, M., "An Algorithm for Unsteady Viscous Flows at All Speeds," *International Journal for Numerical Methods in Fluids*, Vol. 34, No. 5, 2000, pp. 371–401. doi:10.1002/(ISSN)1097-0363

[26] Pearcey, H. H., and Holder, D. W., "Simple Methods for the Prediction of Wing Buffeting Resulting from Bubble Type Separation," Aero Rept. 1024, National Physical Laboratory, 1962.

[27] Iovnovich, M., and Raveh, D. E., "Reynolds-Averaged Navier–Stokes Study of the Shock-Buffet Instability Mechanism," *AIAA Journal*, Vol. 50, No. 4, 2012, pp. 880–890. doi:10.2514/1.J051329

[28] Jacquin, L., Molton, P., Deck, S., Maury, B., and Soulevant, D., "An Experimental Study of Shock Oscillation over a Transonic Supercritical Profile," AIAA Paper 2003-4902, 2005.

[29] Huang, J., Xiao, Z., Liu, J., and Fu, S., "Simulation of Shock Wave Buffet and Its Suppression on an OAT15A Supercritical Airfoil by IDDES," *Science China Physics, Mechanics and Astronomy*, Vol. 55, No. 2, 2012, pp. 260–271. doi:10.1007/s11433-011-4601-9

[30] Crouch, J. D., Garbaruk, A., and Magidov, D., "Predicting the Onset of Flow Unsteadiness Based on Global Instability," *Journal of Computational Physics*, Vol. 224, No. 2, 2007, pp. 924–940. doi:10.1016/j.jcp.2006.10.035

[31] Mettot, C., Renac, F., and Sipp, D., "Computation of Eigenvalue Sensitivity to Base Flow Modifications in a Discrete Framework: Application to Open-Loop Control," *Journal of Computational Physics*, Vol. 269, July 2014, pp. 234–258. doi:10.1016/j.jcp.2014.03.022

[32] Lehoucq, R., Sorensen, D., and Yang, C., *Arpack User's Guide: Solution of Large-Scale Eigenvalue Problems with Implicitly Restarted Arnoldi Methods*, No. 6, SIAM, Philadelphia, 1998, pp. 1–78.

[33] Sipp, D., and Lebedev, A., "Global Stability of Base and Mean Flows: A General Approach and Its Applications to Cylinder and Open Cavity Flows," *Journal of Fluid Mechanics*, Vol. 593, Dec. 2007, pp. 333–358. doi:10.1017/S0022112007008907

[34] Barkley, D., "Linear Analysis of the Cylinder Wake Mean Flow," *EPL (Europhysics Letters)*, Vol. 75, No. 5, 2006, pp. 750–756. doi:10.1209/epl/i2006-10168-7

[35] Mettot, C., Sipp, D., and Bézard, H., "Quasi-Laminar Stability and Sensitivity Analyses for Turbulent Flows: Prediction of Low-Frequency Unsteadiness and Passive Control," *Physics of Fluids*, Vol. 26, No. 4, 2014, Paper 045112. doi:10.1063/1.4872225

[36] Marquet, O., Lombardi, M., Chomaz, J., Sipp, D., and Jacquin, L., "Direct and Adjoint Global Modes of a Recirculation Bubble: Lift-up and Convective Non-Normalities," *Journal of Fluid Mechanics*, Vol. 622, March 2009, pp. 1–21. doi:10.1017/S0022112008004023

[37] Liepmann, H. H. W., *Elements of Gas Dynamics*, Courier Dover, New York, 1957, pp. 284–304.

[38] Agostini, L., Larchevêque, L., Dupont, P., Debiève, J. F., and Dussauge, J. P., "Zones of Influence and Shock Motion in a Shock/Boundary-Layer Interaction," *AIAA Journal*, Vol. 50, No. 6, 2012, pp. 1377–1387. doi:10.2514/1.J051516

[39] Giles, M. B., and Pierce, N. A., "Adjoint Equations in CFD: Duality, Boundary Conditions and Solution Behaviour," AIAA Paper 1997-1850, 1997.

[40] Giles, M. B., and Pierce, N. A., "Analytic Adjoint Solutions for the Quasi-One-Dimensional Euler Equations," *Journal of Fluid Mechanics*, Vol. 426, No. 2001, 2001, pp. 327–345. doi:10.1017/S0022112000002366

[41] Hill, D. C., "A Theoretical Approach for Analyzing the Restabilization of Wakes," AIAA Paper 1992-0067, 1992.

[42] Bottaro, A., Corbett, P., and Luchini, P., "The Effect of Base Flow Variation on Flow Stability," *Journal of Fluid Mechanics*, Vol. 476, Feb. 2003, pp. 293–302. doi:10.1017/S002211200200318X

[43] Farrell, B. F., and Ioannou, P. J., "Generalized Stability Theory. Part I: Autonomous Operators," *Journal of the Atmospheric Sciences*, Vol. 53, No. 14, 1996, pp. 2025–2040. doi:10.1175/1520-0469(1996)053<2025:GSTPIA>2.0.CO;2

[44] Jovanovic, M. R., and Bamieh, B., "Componentwise Energy Amplification in Channel Flows," *Journal of Fluid Mechanics*, Vol. 534, July 2005, pp. 145–183. doi:10.1017/S0022112005004295

[45] McKeon, B. J., and Sharma, A. S., "A Critical-Layer Framework for Turbulent Pipe Flow," *Journal of Fluid Mechanics*, Vol. 658, No. 1, 2010, pp. 336–382. doi:10.1017/S002211201000176X

[46] Brandt, L., Sipp, D., Pralits, J. O., and Marquet, O., "Effect of Base-Flow Variation in Noise Amplifiers: The Flat-Plate Boundary Layer," *Journal of Fluid Mechanics*, Vol. 687, Nov. 2011, pp. 503–528. doi:10.1017/jfm.2011.382

[47] Garnaud, X., Lesshafft, L., Schmid, P. J., and Huerre, P., "The Preferred Mode of Incompressible Jets: Linear Frequency Response Analysis," *Journal of Fluid Mechanics*, Vol. 716, Feb. 2013, pp. 189–202. doi:10.1017/jfm.2012.540

[48] Plotkin, K. J., "Shock Wave Oscillation Driven by Turbulent Boundary-Layer Fluctuations," *AIAA Journal*, Vol. 13, No. 8, 1975, pp. 1036–1040. doi:10.2514/3.60501

[49] Touber, E., and Sandham, N. D., "Low-Order Stochastic Modelling of Low-Frequency Motions in Reflected Shock-Wave/Boundary-Layer Interactions," *Journal of Fluid Mechanics*, Vol. 671, March 2011, pp. 417–465. doi:10.1017/S0022112010005811

[50] Sipp, D., and Marquet, O., "Characterization of Noise Amplifiers with Global Singular Modes: The Case of the Leading-Edge Flat-Plate Boundary Layer," *Theoretical and Computational Fluid Dynamics*, Vol. 27, No. 5, 2013, pp. 617–635. doi:10.1007/s00162-012-0265-y

M. Choudhari
Associate Editor